# Structural design and particle size examination on NiO-CeO$_2$ catalysts supported on 3D-printed carbon monoliths for CO$_2$ methanation

Iván Martínez-López [a], José Clemencio Martínez-Fuentes [a], Juan Bueno-Ferrer [a], Arantxa Davó-Quiñonero [a,*], Esteban Guillén-Bas [a], Esther Bailón-García [b], Dolores Lozano-Castelló [a], Agustín Bueno-López [a,*]

[a] *Department of Inorganic Chemistry, University of Alicante, Carretera de San Vicente s/n, Alicante, Spain*
[b] *Department of Inorganic Chemistry, University of Granada, Avenida de la Fuente Nueva s/n, Granada, Spain*

## ARTICLE INFO

## ABSTRACT

3D-printed high-surface carbon monoliths have been fabricated and tested as catalyst supports of CO$_2$ methanation active phases (NiO-CeO$_2$, 12 wt% Ni). The carbon carriers show a developed microporosity and good adherence to the catalytic phases of NiO-CeO$_2$, showing great stability and cyclability. Two monolith designs were used: a conventional parallel-channeled structure (honeycomb) and a complex 3D network of non-linear channels built upon interconnected circular sections (circles), where flow turbulences along the reactant gas path are spurred. The effect of the active phases particle size on the catalyst distribution and the overall performance has been assessed by comparing NiO-CeO$_2$ nanoparticles of 7 nm average (Np), with a reference counterpart of uncontrolled structure (Ref). The improved radial gases diffusion in the circles monolith design is confirmed, and nanoparticles show enhanced CO$_2$ methanation activity than the uncontrolled-size active phase at low temperatures ($< 300$ ºC). On the contrary, the Ref catalysts achieve higher CH$_4$ production at higher temperatures, where the reaction kinetics is controlled by mass transfer limitations (T $> 300$ ºC). SEM and Hg porosimetry evidence that nanoparticles are deposited at deeper penetration through the narrow micropores of the carbon matrix of the monolithic supports, which tend to accumulate on the channels surface remaining more accessible to the reactant molecules. Altogether, this study examines the impact of the channel tortuosity and the active phase sizing on the CO$_2$ methanation activity, serving as ground knowledge for the further rational and scalable fabrication of carbon monolith for catalytic applications.

## 1. Introduction

Initiatives to mitigate CO$_2$ emissions are urgently demanded amid the global emergency to front climate change. Strategies to capture and convert CO$_2$ into added-value products have been set as a primary focus in environmental and energy research. In this context, the CO$_2$ hydrogenation to methane is gaining increasing attention [1–5]. Although the CO$_2$ methanation is known since the early twentieth century, it is now being proposed as an efficient route to reduce CO$_2$ emissions while producing a valuable fuel of relevance in the energy mix, such as CH$_4$, or synthetic natural gas [6,7].

CO$_2$ methanation is thermodynamically favored at low temperature but kinetically restricted, so a catalyst is required to achieve sufficient reaction rates with industrial relevance at economically practicable temperatures. Among the CO$_2$ methanation active metals, nickel nanoparticles are claimed to be a good option with an operativity between 200 and 400 °C, besides the advantage of its moderate price in comparison to noble metals [8–13]. When loaded into ceria-based carriers, the activity of nickel is promoted as Ni-Ce interfacial redox interplay facilitate both CO$_2$ activation and H$_2$ dissociation [14–16]. Thus, the rational design in the synthesis of NiO-CeO$_2$ systems and the occurring CO$_2$ methanation mechanisms have been studied in detail. It has been reported that reduced Ni particles are efficient sites for H$_2$ dissociation, while CO$_2$ activation mainly occurs at oxygen vacancies located at the NiO-CeO$_2$ interface. The proportion of the two types of sites rules the overall catalytic performance, which can be adjusted to achieve an optimum by means of tuning the nanostructure of the dispersed phases [17].

---

* Corresponding authors.
*E-mail addresses:* arantxa.davo@ua.es (A. Davó-Quiñonero), agus@ua.es (A. Bueno-López).

As a structure-sensitive reaction, the size of catalyst nanoparticles can determine the $CO_2$ methanation activity and selectivity given that the surface structure and electronic properties change in this size range [18–20]. NiO-CeO$_2$ nanoparticles are highly stable under reaction conditions and active for $CO_2$ hydrogenation at low temperature (T $\geq$ 200–250 ºC) with selectivity towards $CH_4$ near ~100% [21].

Besides controlling the microstructural features of the active phases, the configurational aspects of the catalytic bed must be carefully considered when designing a catalytic process. When high flows are demanded, monolithic structures are preferred when compared to powder-packed beds to avoid pressure drop in the reactors. Monolithic catalysts enable a facile scale-up and are easily replaced while avoid degradation by friction occurring in packed beds. Ceramic monoliths, typically based on cordierite, are extensively used as catalytic supports in a variety of industrial applications, such as catalytic combustion, volatile organic compound oxidation or soot combustion among others [22–24]. These materials present a high mechanical strength, thermal stability that provide versatility in use, besides an easy cleaning and replacement [25]. However, the surface properties of ceramic-based monoliths, such as porosity and surface chemistry can only be barely modified. In contrast, carbon materials possess unique characteristics that point them as suitable candidates for a wide range of applications, including adsorption, gas separation, or in chemical reactions serving either as catalysts or as catalyst supports. Carbon materials can be synthesized with high surface area and pore volume, large stability, and adaptability due to their great tailoring possibilities on their textural properties and chemical features [26,27]. As a result, carbon monoliths have been successfully proposed for various applications and have demonstrated their promising potential [28,29].

Carbon honeycomb monoliths are usually made from a paste containing a precursor, a binder, and an organic or inorganic filler, and are manufactured by extrusion. Once dried, the materials are carbonized to produce a porous carbon monolith. To avoid shrinkage, carbon materials can be combined with ceramic binders to provide sufficient strength and stability [30–32]. Regardless of the strategy used to fabricate the carbon monolith, the channel morphology is limited to straight lines rather than complex designs due to the extrusion technique. Alternative designs can lead to important advances in catalysis by enabling a better use of the often-expensive active phases. Conventional honeycomb monoliths force the laminar fluid to flow through straight channels, causing radial mass transfer limitations that lead to unfavorable active phase–reagent contacts and thus loss of activity. Thus, modifications in the channel design, which may induce turbulent flow in the channels, have demonstrated to be promoters of active phase-reactant interactions that eventually improve catalytic performance [33]. Advanced designs cannot be manufactured using conventional extrusion techniques. However, nowadays 3D printing can take us further in this field.

Previous investigations of our research group lead to the manufacture of carbon monoliths combining 3D printing and sol-gel techniques [34–36]. Polymeric molds were printed with channels of various geometries, which were then filled with a carbon gel precursor, a resorcinol-formaldehyde solution. After polymerization, gelation, and solidification, the resin is carbonized to obtain the mold-free carbon monoliths. This manufacture pathway opened a window of numerous possibilities when designing the structure of the monoliths [37]. One of the milestones of this technology was the fabrication of integral carbon monolithic supports for NiO-CeO$_2$ $CO_2$ methanation catalysts [36]. In this study, it was found that the tunable textural properties of the carbonaceous supports directed the NiO-CeO$_2$ dispersion and, in turn, the interfacial Ni/NiO/CeO$_2$ redox interplay and synergistic interactions. Compared to pure powdered NiO-CeO$_2$, the structured NiO-CeO$_2$ on carbon monoliths exhibited enhanced reducibility by the effect of the intimate contact with carbon, while crystalline features of NiO-CeO$_2$ remained unaltered.

With this know-how in the background, we herein take a step forward toward the fine tuning of the carbon monoliths as catalyst supports for $CO_2$ methanation. On the one hand, a novel monolith design built upon interconnected circular sections is tested and compared to standard honeycomb counterpart. On the other hand, for the first time the effect of the microstructure of NiO-CeO$_2$ active phases in the catalyst-carbon contact and catalytic behavior has been addressed. We have focused on NiO-CeO$_2$ (12 wt% Ni) mixed oxide prepared by microemulsion and by direct calcination of the metal precursors to obtain active phases with narrow nanoparticle size and without control of the particle size, respectively. They were supported on the porous carbon monoliths, and the notorious influence of the particle size of the inorganics deposition and eventual catalytic performance has been unraveled. This study adds valuable insights to the rational design of custom adapted synthesis and utilization of porous carbon monoliths as catalyst carriers for a greener future.

## 2. Experimental details

### 2.1. Catalysts preparation

Ce(NO$_3$)$_3$·6 H$_2$O (99.5%, Alfa Aesar) and Ni(NO$_3$)$_2$·6 H$_2$O (Panreac) were chosen as metal precursors of Ce and Ni, respectively. Herein, four catalysts have been prepared, characterized and tested in $CO_2$ methanation reaction by combining NiO-CeO$_2$ active phases of different particle size, both with 12 wt% of Ni, and two monolithic carbon supports with two different channel designs. The samples nomenclature and their synthesis parameters are defined as follows.

#### 2.1.1. NiO-CeO$_2$ (Ref)

The CeO$_2$ support of the reference material was prepared by calcining the cerium precursor at 500 °C for 1 h. Ni was loaded into the CeO$_2$ support by incipient wetness impregnation of aqueous solution of the Ni precursor. After the impregnation the resulting solid was calcined at 500 °C for 1 h.

#### 2.1.2. NiO-CeO$_2$ (Np)

NiO-CeO$_2$ nanoparticles were synthesized by the reverse microemulsion method [38], involving the preparation of two microemulsions. The first one contains the metal precursors (1.18 g of Ni precursor and 4.27 g of Ce precursor) dissolved in 20 mL of water, 114 g of n-heptane, 37 g of surfactant (Triton X-100) and 29 g of hexanol as co-surfactant. The second microemulsion was prepared using the same solvents and surfactants but adding 6.8 g of tetramethyl ammonium hydroxide pentahydrate instead of the metal precursors. Both microemulsions were mixed and vigorously stirred for 24 h. After precipitation, the suspension was centrifuged and the solid was washed with ethanol, dried at 110 °C and calcined at 500 °C for 1 h. This synthesis route leads to the formation of uniform, stable and active NiO-CeO$_2$ nanoparticles, as previously reported by our group [21].

#### 2.1.3. Carbon monoliths preparation

The carbon monoliths were synthesized by sol-gel polymerization. Firstly, the polymeric templates were designed with a 3D computer program Cubify Invent (Fig. 1a) and printed using a 3D-printer Ultimaker with UltiMaker CPE+ (co-polyester) filament (Fig. 1b). The polymeric templates were created in two different designs: a conventional honeycomb design composed of straight channels (Fig. 1b left; referred to as "honeycomb") and a complex design with a 3D network of nonlinear channels of circular interconnections (Fig. 1b right; referred to as "circles"). This design forces the reactive gas to converge and diverge at the junctions of the circular channels. The tortuous gas path along the monolith disturbs the laminar flow and promotes the turbulence, which enhances the radial diffusion of the reactant phase towards the catalytic layer [39,40].

The templates were placed in glass tubes and filled with a mixture of resorcinol, formaldehyde and water in 1:2:15 molar ratio. The tubes
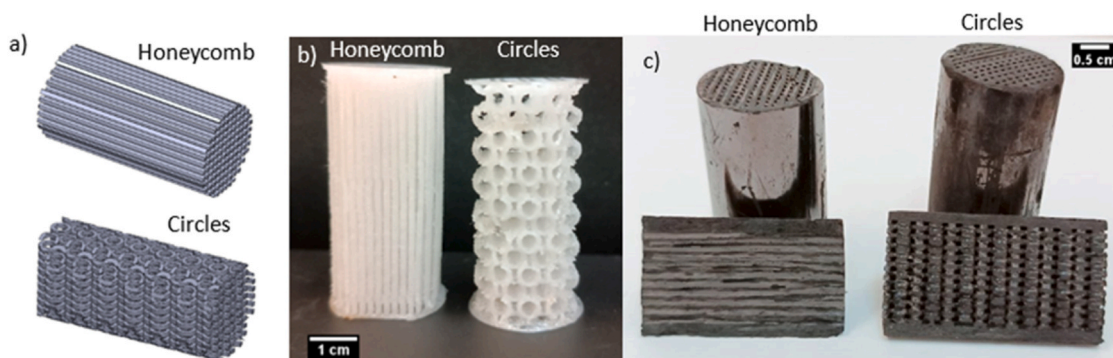
**Fig. 1.** (a) Computer design of the templates; (b) CPE monolith templates manufactured by 3D printing; (c) carbon monoliths.

were sealed and polymerization was carried out at room temperature for 24 h, then 50 °C for 24 h, and finally, 80 °C for 120 h (5 additional days). The cured gel was unmolded and immersed in acetone for 3 days to replace the pore water with acetone and facilitate the drying process avoiding porosity collapse. Finally, the green monoliths were carbonized at 900 °C for 2 h at a heating rate of 3 °C $min^{-1}$ in $N_2$ atmosphere. The pieces suffered an important contraction upon carbonization, namely a decrease in width of 19% and length of 20%. The final dimensions of the carbon monoliths (Fig. 1c) were 2.2 cm diameter × 3.8 cm length.

### 2.1.4. Active-phase loading

Four catalysts were prepared, which are denoted as $NiO-CeO_2$ (Ref) honeycomb, $NiO-CeO_2$ (Np) honeycomb, $NiO-CeO_2$ (Ref) circles and $NiO-CeO_2$ (Np) circles. The $NiO-CeO_2$ active phases were loaded on the carbon monoliths by drop-by-drop impregnation using ethanolic suspensions (15 wt%) with the aim to avoid an undesired blockage of the channels, expected to occur in monoliths with unconventional geometries upon their immersion into the wash coat solutions. In such tortuous channel configurations, dip-coating methods followed by air blowing fail to provide an even active phases distribution evenly along the monolith length. The impregnated monoliths were dried for 2 h at 100 ºC and impregnation was repeated until the nominal load of 200 mg of active phase was achieved on each support. Last drying step was carried out at room temperature rotating the monoliths in horizontal position to promote active phase dispersion into the whole carbon support. Finally, the active phase-containing monoliths were heat treated at 500 °C in inert atmosphere of $N_2$ for 1 h at a heating rate of 3 °C $min^{-1}$. The final amount of active phase loaded on the monoliths was 200 ± 10 mg.

### 2.2. $CO_2$ methanation tests

The catalytic performance was analyzed in the $CO_2$ methanation reaction. A fixed-bed 2.7 cm inner diameter stainless-steel cylindrical reactor was used. The carbon monoliths were placed inside the reactor using aluminum foil to seal the space between the external wall of the monoliths and the reactor to avoid the gas to flow through the outer non-catalytic surface. The outlet gas composition was monitored during the experiments using a set of NDIR-UV gas analyzers AwiFLEX Cool+ for CO, $CO_2$ and $CH_4$, and an electrochemical sensor for $H_2$.

Experiments were performed with total reaction gas mixture flows between 100 and 500 mL/min and a stoichiometric composition of 10% $CO_2$, 40% $H_2$, and 50% $N_2$ at 1 bar of total pressure Before the reaction, the catalysts were reduced in situ at 400 °C for 1 h with 200 mL/min of 50% $H_2$ and 50% $N_2$ mixture. Steady state lectures of the gas composition were taken at different temperatures.

The effect of reactants partial pressures was studied at 275 ºC and 300 ºC fixing a flow rate of 200 mL/min and varying the inlet partial pressures of $CO_2$ and $H_2$ always maintaining a 1:4 $CO_2$ to $H_2$ ratio in the total gas flow.

### 2.3. Catalyst characterization

Gas adsorption measurements were carried out with $N_2$ at −196 °C and $CO_2$ at 0 °C using a Quantachrome Autosorb-6B equipment to obtain information about the porosity of the materials. The samples were ground for these measurements and degassed at 200 °C for 4 h before the gas adsorption experiments. Hg porosimetry was carried out on a Poremaster 60 GT (Quantachrome) using the grounded samples previously outgassed at 110 °C for 12 h.

TEM images of the active phases were obtained in a JEOL microscope, model JEM-2010. The active phases particle size distribution was measured from TEM images with the program ImageJ using, at least, 100 particles of each active phase. SEM images of the monolith catalysts were captured with the FESEM Zeiss microscope, model Merlin VP Compact. X-ray diffractograms (XRD) were obtained in a Bruker D8-Advance diffractometer, working with Cu Kα radiation (λ = 1.540598 Å). The diffractograms were recorded using grounded samples, with a step size of 0.025° and a recording time of 3 s per step.

## 3. Results and discussion

### 3.1. $CO_2$ methanation tests

Fig. 2 shows the $CO_2$ conversion profiles of the prepared catalysts in the $CO_2$ methanation catalytic tests conducted with 100 mL/min of total gas flow.

The $CO_2$ conversion ($X_{CO_2}$) profiles depicted in Fig. 2 show that the four structured $NiO-CeO_2$ catalysts present an outstanding $CO_2$ methanation activity. The selectivity of all four catalysts is ~100% to $CH_4$. The bare carbon monoliths do not present $CO_2$ methanation activity, so the catalytic performance relies on the $NiO-CeO_2$ sites. The swift divergence of the $CO_2$ conversion ($X_{CO_2}$) profiles as temperature increases reveals a moderate but noticeable improvement in the $CO_2$ methanation performance of the monolith with circular structure with regards to honeycomb counterparts. As temperature increases, intrinsic kinetics accelerate, and beyond a certain temperature, diffusion (i.e., mass transfer) limits the overall reaction rate. The beneficial support effect is ascribed to the different gas diffusional features throughout the monolith lengths. Namely, the circular monoliths are expected to improve the gas phase radial mixing as laminar flow is continuously disrupted by the tortuous channel design, which is a catalytic advantage when the reaction kinetics is ruled by diffusion.

Regardless of the channel structure, $NiO-CeO_2$ (Np) containing catalysts present an intrinsic higher activity than those with $NiO-CeO_2$ (Ref), in accordance with our previous results that evidenced the higher activity of nanoparticles [17]. Such differences are more evident at increasing the total flow above 100 mL/min, as intrinsic kinetics becomes more determining in the overall rate control. As seen in Fig. 3, below 300 °C, higher $CO_2$ methanation rates are achieved by nanoparticles but increasing the temperature beyond 300 °C leads to the
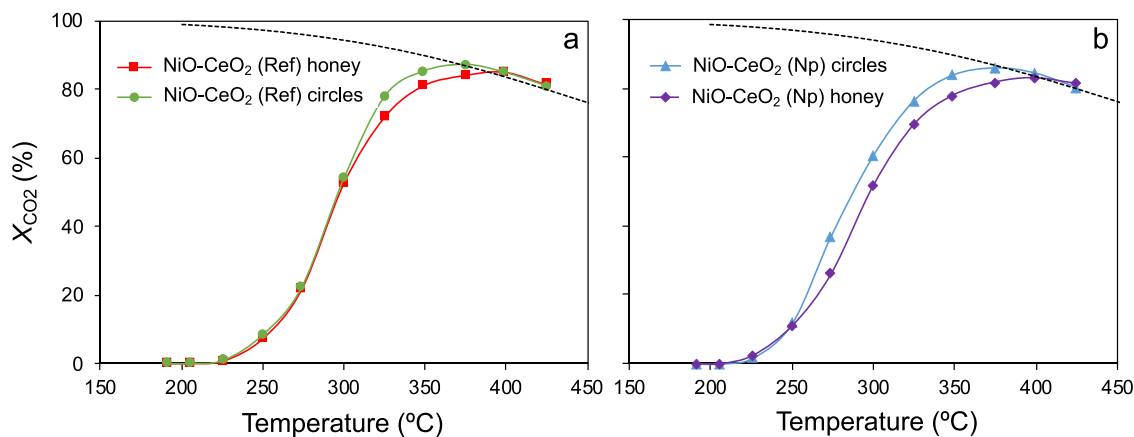
**Fig. 2.** $CO_2$ conversion ($X_{CO2}$) profiles in $CO_2$ methanation experiments with (a) $NiO$-$CeO_2$ reference and (b) $NiO$-$CeO_2$ nanoparticles catalysts supported on the different designs. Reaction conditions: Total gas flow 100 mL/min; 10% $CO_2$ + 40% $H_2$ + 50% $N_2$. Pre-treatment: 400 °C/1 h; 200 mL/min; 50% $H_2$ + 50% $N_2$, 1 bar. Dotted line stands for the thermodynamic limit according to the reaction conditions.
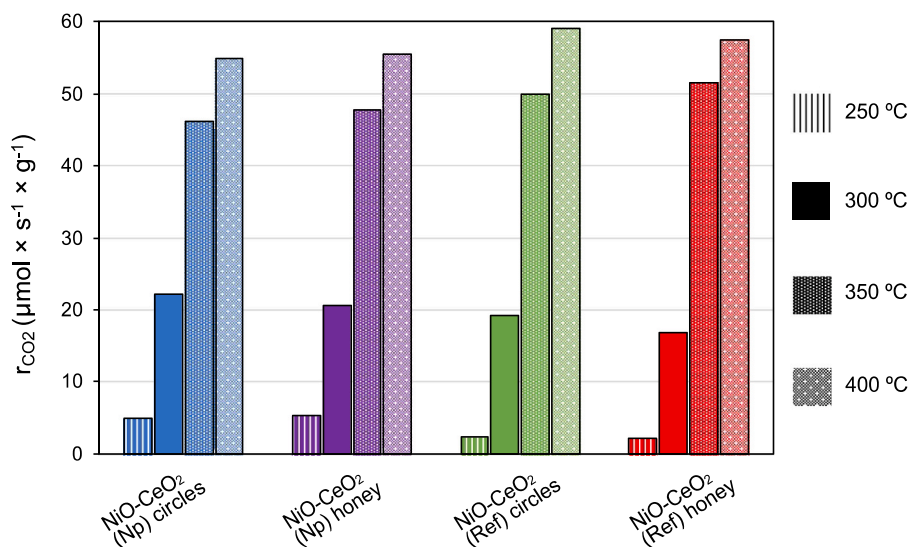


**Fig. 3.** $CO_2$ methanation rate achieved by the catalysts at different temperatures. Total gas flow 200 mL/min; 10% $CO_2$ + 40% $H_2$ + 50% $N_2$, 1 bar. Pre-treatment: 400 °C/1 h; 200 mL/min; 50% $H_2$ + 50% $N_2$.

opposite behavior with $NiO$-$CeO_2$ (Ref) moderately outperforming. This is attributed to the fact that nanoparticles are sparsely located through the carbon matrix, in contrast to the active phase prepared without control of the size, which is preferentially located at the channel surface. Thus, nanoparticles end up being partially inaccessible to the gas, which turns detrimental at high intrinsic chemical rates as diffusional limitations through the ultra-microporous carbon matrix arise. $NiO$-$CeO_2$ (Ref) particles tend to remain closer to the surface of the channels, where the reactant gas can flow through swiftly reaching a larger fraction of the active sites. In agreement with this, we previously reported for analogous systems that though gases mainly flow through the monolith channels, it can also diffuse into the porous structure of carbon up to a certain extent depending on specific porosity aspects [31,32].

Herein, it is important to discern between internal diffusion and external mass transfer concepts. The latter, based on convection and advection phenomena, can be optimized by the experimental conditions. However, the diffusive mass transport into the pores cannot be neither easily assessed nor tuned, as it depends on factors such as: structural features of the catalyst, pore wall-gas interactions or the inherent gas diffusivities, which can limit the overall catalytic yield when diffusion is inefficient [41].

In order to shed some light, Arrhenius plots have been realized by

representing the apparent activation energy of the mean reaction rate as a function of 1/T (Fig. 4). Since $CO_2$ methanation is assumed to be order near-zero with respect to $CO_2$ and $H_2$ in related systems, the $CO_2$ methanation kinetic rates can be approximated to the apparent coefficient rate to build Arrhenius plots [42,43]. Arrhenius plots enable to elucidate whether diffusional restrictions are at play under different conditions, since mass transfer and diffusion are not that strongly influenced by temperature as the reaction kinetics. A change in the slope of the Arrhenius plot to near the half of the one under kinetic control regime ($E_{a,diff} = 0.5 \times E_{a,kin}$) evidences that the temperature range where reaction rate is limited by internal diffusion [44,45]. At higher temperatures, the slope of the Arrhenius plots tends to decrease towards a near-negligible value when it is dominated by mass transfer kinetic limitations, since bulk transport of the gas phase is only weakly dependent on temperature. In the case of the powder active phases (see Fig. 4a and b), the reference material displays a temperature region (between 250 and 290 °C) where internal diffusional limitations govern the overall methanation kinetics. On the contrary, in the nano-sized $NiO$-$CeO_2$ (in Fig. 4b), the kinetics reach the mass transport limits beyond 250 °C. This is consistent with the structural features of the corresponding active phases, as the significant decrease in particle size of $NiO$-$CeO_2$ (Np) with regards to $NiO$-$CeO_2$ (Ref) reduces internal
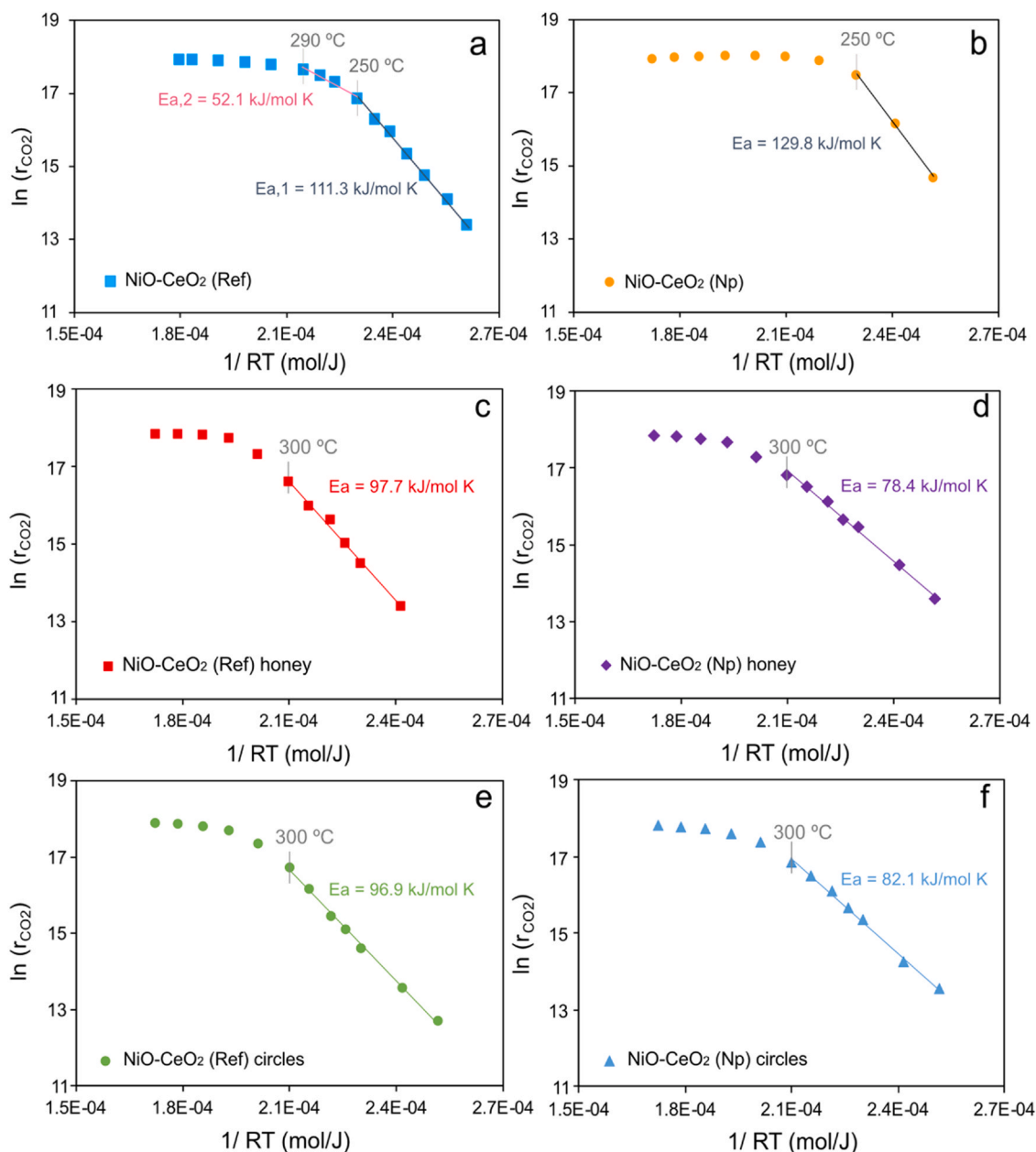
**Fig. 4.** Arrhenius plots of the catalytic outputs in $CO_2$ methanation tests performed with 200 mL/min of total flow using (a) NiO-CeO$_2$ (Ref), (b) NiO-CeO$_2$ (Np), (c) NiO-CeO$_2$ (Ref) honeycomb, (d) NiO-CeO$_2$ (Np) honeycomb, (e) NiO-CeO$_2$ (Ref) circles and (f) NiO-CeO$_2$ (Np) circles.

diffusion problems because of the superior exposed area of the former. Activation energies are in agreement with the published literature for Ni-Ce systems [43,46–49], although the apparent activation energy of NiO-CeO$_2$ (Np) is slightly above the average.

Arrhenius plots of the monolithic catalysts are shown in Fig. 4c–f. Trendlines show quadratic regression coefficients ($R^2$) above 0.99, which indicates that data adjustment is reliable. The moderate deviations of the linearities are attributed to the slight divergence from zero of the global order of reaction, as assumed in the approximation [50]. In the four catalysts prepared, it can be depicted that the transition to mass transfer control occurs at 300 °C. This confirms that NiO-CeO$_2$ (Np) exhibits better catalytic performance than NiO-CeO$_2$ (Ref) in the range where intrinsic kinetics control prevails. On the contrary, at higher temperatures (T > 325 °C), where the rate is controlled by external mass transfer limitations, the catalysts with NiO-CeO$_2$ (Ref) active phase achieve higher conversions than those loaded with NiO--CeO$_2$ (Np), as seen in Fig. 3.

The activation energies obtained for the monolithic catalysts are in good agreement with literature [43,46], and they reveal that the effect of active phase prevails when compared to monolith design. Thus, nanoparticles and reference-based catalysts present similar apparent activation energies in between regardless of the monolith design. Namely, NiO-CeO$_2$ (Np) catalysts display moderately lower activation energies than NiO-CeO$_2$ (Ref), which can be tentatively ascribed to the presence of internal diffusion constrains in agreement to the higher dispersion of nanoparticles in the carbon matrix. Comparing with the corresponding powder catalysts, the monolithic catalysts show lower activation energies, falling also in the range of the reported values for analog active phases. The disagreements (powder to monolith) encountered can be ascribed to potential heat dissipation limitations in the packed-bed reactor containing the powder catalyst, as heat transfer problems tend to increase activation energies. $CO_2$ methanation is a highly exothermic reaction and it is well-known it requires of an efficient heat management to prevent hotspots and temperature excursions

that could alter methane production yield by approaching the thermodynamic equilibrium and cause thermal stress on the catalyst [51,52]. While in the powder catalysts, a generous amount of SiC is mixed with the catalyst (10:1 ratio) in the packed bed to act as heat dissipator, in the monolithic catalysts, the bulky carbon-based supports disperse the NiO-CeO$_2$ particles within their volume, so that the heat effects by the intrinsic exothermicity are minimized. This another advantageous aspect is of practical interest in the use of carbon monoliths loaded with disperse active phase in exothermic reactions.

The behavioral changes of the catalysts have been further addressed by studying the transitions of the reaction rate control regimes in catalytic CO$_2$ methanation experiments. To do so, catalytic tests have been performed using different total gas flows keeping in all cases the 4:1 to H$_2$ to CO$_2$ stoichiometric ratio (Fig. 5).

Fig. 5 reveals the effect of temperature, active phase and monolith design in the kinetic control transition. The criterion for no external mass transfer limitations relies on the independence of the reaction rate on the gas linear velocity at constant space velocity [53–55]. The catalytic tests conducted on the carbon monoliths at different flow rates depicted in Fig. 5 serve as a rough approximation to assess transport limitations, given that gases-catalyst contact time is diminished when increasing flows as monolith lengths are a fixed parameter. Thus, although this approach is not precise when in intrinsic kinetics and internal diffusional control by the variability on the mass transfer coefficients, as seen by the moderate linearities, the change of slope of the trend lines unequivocally reveal the domain of mass transfer rate control. At the temperature of 275 ℃ (open symbols), most of the catalysts perform without mass transfer kinetic limitations with the exception of NiO-CeO$_2$ (Np) honeycomb at the lowest flow of 100 mL/min. On the

contrary, at 300 ℃, the intrinsic reaction rate is higher than that of 275 ℃ and the overall rate control is in transition to the mass transfer control threshold, in agreement with the breakings found in the slope of the Arrhenius plots (Fig. 4). In the case of the honeycomb catalysts (Fig. 5a), the prevailing kinetic regime with the NiO-CeO$_2$ (Ref) active phase is mass transfer control in the full set of experiments with flows 100–500 mL/min. However, in the case of the NiO-CeO$_2$ (Np) active phase, the CO$_2$ methanation reaction is controlled by intrinsic kinetics beyond 100 mL/min, an analog behavior to the observed at 275 ℃ for the same catalyst. Thus, in the honeycomb-type monolith supports structured by a parallel channel array, the deeper penetrability of the NiO-CeO$_2$ (Np) active phase into the microporous carbon matrix results detrimental as it reduces the availability of active sites decreasing the expected intrinsic kinetics when compared to NiO-CeO$_2$ (Ref) on the same support. This aspect is especially relevant at higher flows, where internal gas diffusion throughout the narrow micropores of carbon is compromised.

In the case of NiO-CeO$_2$ (Np) circles, the catalyst performs under kinetic control at the highest flow 500 mL/min at 300 ℃, in contrast to NiO-CeO$_2$ (Ref) circles catalyst, which performs under mass transfer control in the whole range of flow rates tested. This is attributed to the lesser availability of the NiO-CeO$_2$ (Np) active phase on the accessible surface, as explained above. The comparison with the behavior at 275 ℃ in Fig. 5b, when both circles catalysts perform under intrinsic kinetic control confirms 300 ℃ as the kinetic regime transition point.

As a complementary check, experiments with different gas mixture (CO$_2$ + H$_2$) concentration in the total flow (200 mL/min) at a fixed inlet CO$_2$:H$_2$ ratio of 1:4 were conducted at 275 and 300 ℃ (Fig. 6). Linear trends in the plot $r_{CO2}$ (CO$_2$ methanation rate) versus $p_{CO2}$ (and $p_{H2}$, proportionally) depict intrinsic kinetic control as the overall reaction rate is ruled by the general kinetic equation $r = k \times [p_{CO2}]^a \times [p_{H2}]^b$, being $a + b < 1$. On the contrary, curved trends ascribed to breakings in the kinetic equation reveal mass transfer rate limitations, as observed for
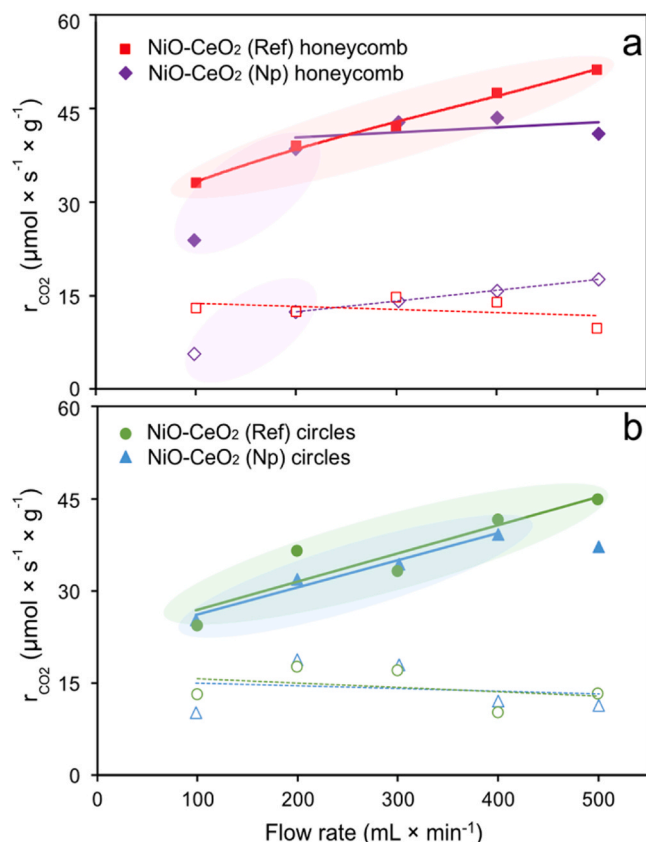
**Fig. 5.** CO$_2$ methanation rates achieved in fixed-bed catalytic tests with NiO-CeO$_2$ (Ref) and NiO-CeO$_2$ (Np) honeycomb (a) and circles (b) catalysts with different total gas flows (100–500 mL/min) at 275 ℃ (open symbols) and 300 ℃ (solid symbols). Mass transfer rate control is attained in the shaded conditions.
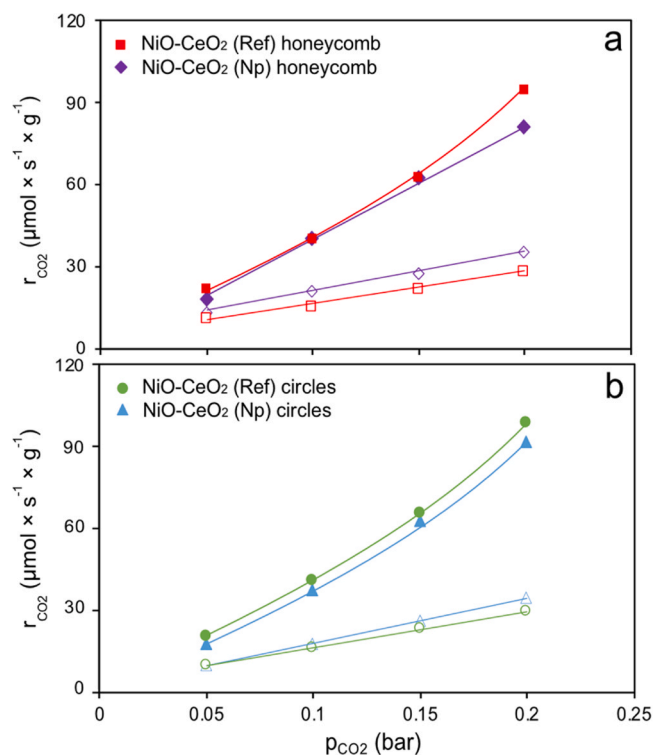
**Fig. 6.** CO$_2$ methanation rates achieved in fixed-bed catalytic tests with NiO-CeO$_2$ (Ref) and NiO-CeO$_2$ (Np) honeycomb (a) and circles (b) catalysts with different CO$_2$ and H$_2$ partial pressures (inlet CO$_2$:H$_2$ ratio fixed at 1:4) under 200 mL/min total flow at 275 ℃ (open symbols) and 300 ℃ (solid symbols).

the circles catalysts and the NiO-CeO$_2$ (Ref) honeycomb at 300 ºC, while NiO-CeO$_2$ (Np) honeycomb is confirmed to perform catalytically under kinetic rate control at 300 ºC. These outputs are in good agreement with the results enclosed in Fig. 5, confirming the catalytic behaviors assessed for each catalyst.

In conclusion, NiO-CeO$_2$ (Np) present higher activity than NiO-CeO$_2$ (Ref), and this leads to higher CO$_2$ conversions to methane at low temperatures when the reaction rate is controlled by intrinsic kinetics. However, the distribution of NiO-CeO$_2$ (Ref) allows to achieve better catalytic results under mass transfer control than smaller nanoparticles occluded into the carbon microporous network. Regarding the monolith design, the circular structure improves the gas radial mixing along the monolith path, allowing to achieve higher CO$_2$ conversion at low flows (100 mL/min) when compared to honeycomb supports. Fig. 5 illustrates that the flowing gas presents higher mass transfer constrains in the circular channels than in the conventional paralleled ones. The lower reaction rates of NiO-CeO$_2$ (Np) honeycomb than that of NiO-CeO$_2$ (Np) circles at high flows, can be attributed to a lower availability of the nano-sized active sites in the circular monolith design owing to its higher bulk carbon density than the honeycomb counterpart.

*3.2. Catalysts characterization*

Fig. 7 shows representative TEM images of the powder active phases at different magnifications, where clear differences are observed between the reference active phase prepared without size control (Fig. 7a, b) and nanoparticles (Fig. 7c, d). Particle size distributions assessed using a large set of TEM images are included in Fig. 7e.
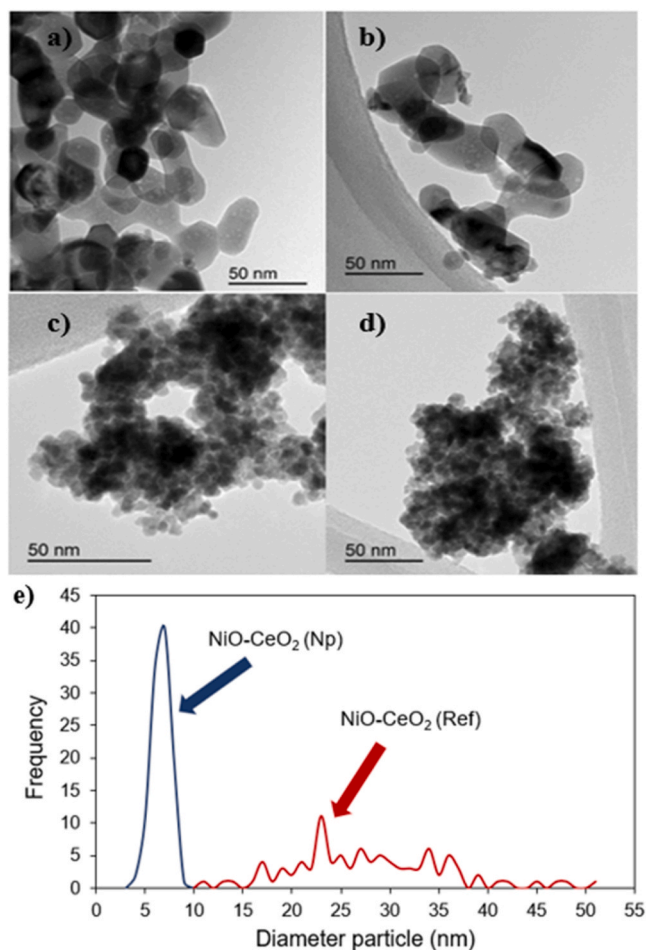


**Fig. 7.** TEM images of the powder active phases (a,b) NiO-CeO$_2$ (Ref), (c,d) NiO-CeO$_2$ (Np) and (e) particle size distribution.

The NiO-CeO$_2$ (Ref) active phase shows a broad size distribution with heterogeneous particles ranging from 10 to 50 nm, the most frequent size being around 23 nm. On the contrary, NiO-CeO$_2$ (Np) shows a narrow particle size distribution around 7 nm. These differences are deemed to determine their penetrability into the microporous carbon matrix of the monoliths support.

Fig. 8 shows representative SEM images of the catalysts, where brighter areas corresponding to the NiO-CeO$_2$ active phases can be discerned from the carbon background. SEM images evidence a heterogeneous distribution of the active phase on the channel surface and within the carbon matrix. When loading NiO-CeO$_2$ (Np) the monolith channels remain emptier since a greater amount of the NiO-CeO$_2$ has penetrated to the carbon microporous network (Fig. 8b, d). On the contrary, NiO-CeO$_2$ (Ref) with a higher average particle size according to TEM images, tends to accumulate on the channels surface building up a more solid catalyst layer on the carbon channels surface, where the reaction gases mainly flow through (Fig. 8a, c).

Hg porosimetry (Fig. 9, Table 1) performed to honeycomb-based catalysts confirms this insight. The pore intrusion profile shows a narrow pore distribution between 1000 and 10,000 nm of the bare carbon monolith. The catalyst loaded with the NiO-CeO$_2$ (Ref) active phase shows a quite similar pore size distribution, evidencing that the carbon macroporosity is only slightly affected upon loading the active phase. On the contrary, NiO-CeO$_2$ (Np) strongly alters the carbon porosity, filling and blocking pores smaller than 5000 nm approximately while generating large new pores of 10,000 nm. Nanopores blocking evidence insertion of nanoparticle clusters into the porosity, and generation of large pores could be tentatively attributed to the local oxidation of the carbon by ceria oxygen during the thermal treatment at 500 ºC.

The textural features were also characterized by isothermal gas physisorption. N$_2$ adsorption-desorption isotherms at –196 ºC (Fig. 10). All isotherms are Type I according to the IUPAC classification, corresponding to microporous materials, in accordance with our previous results [32]. The average pore diameter is around 1.4 nm for all materials (see Table 2). Such narrow average pore diameter hinders N$_2$ diffusion into the carbon matrix, so that obtaining N$_2$ physisorption results of these materials was a challenging endeavor as equilibrium at each N$_2$ dose requested large times. Thus, despite our efforts, in some cases, there is a moderate mismatch between adsorption and desorption branches suggesting that equilibrium state was not fully achieved in adsorption points.
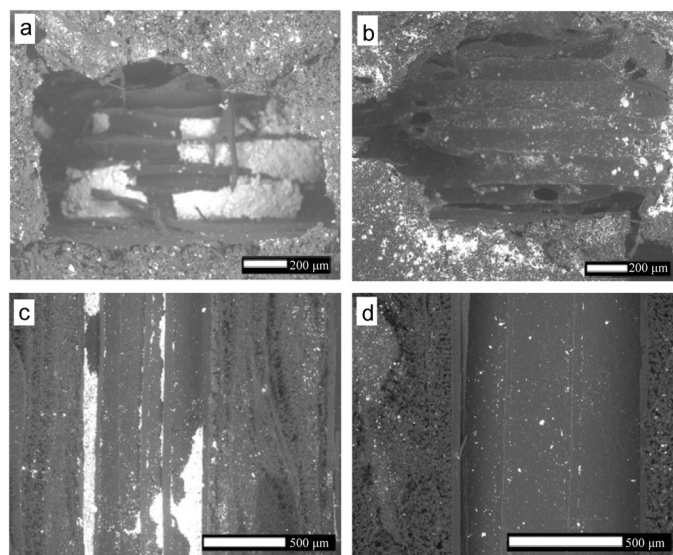


**Fig. 8.** Top view SEM images of (a) NiO-CeO$_2$ (Ref) circles; (b) NiO-CeO$_2$ (Np) circles; and lateral view of (c) NiO-CeO$_2$ (Ref) honeycomb; (d) NiO-CeO$_2$ (Np) honeycomb.
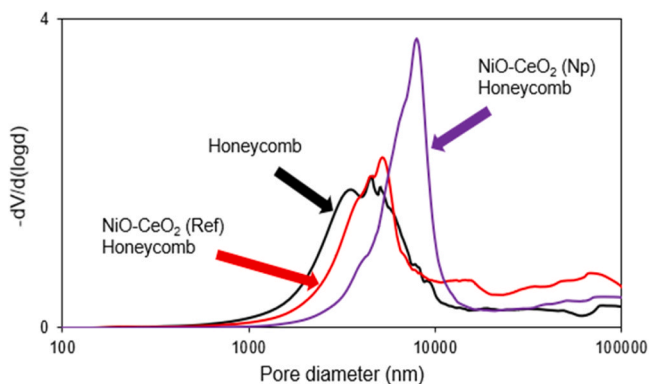
**Fig. 9.** Pore size distribution determined by Hg intrusion porosimetry.

**Table 1**

Macropore volume (50–10,000 nm range) nm determined by Hg intrusion porosimetry.

| Sample | Macropore volume (cm$^3$/g) |
|---|---|
| Honeycomb | 1.01 |
| NiO-CeO$_2$ (Ref) Honeycomb | 0.86 |
| NiO-CeO$_2$ (Np) Honeycomb | 0.98 |

The adsorption on the active phase-free carbon monoliths is different depending on the channels network design, being the "circles" monolith (Fig. 10b) more microporous than the "honeycomb" monolith (Fig. 10a). These differences are also revealed by the calculated BET specific surface areas and pore volumes determined, as displayed in Table 2. Namely, the BET area and pore volume of the circular-based monolith (584 m$^2$/g and 0.37 cm$^3$/g, respectively) are superior to the corresponding values calculated for the honeycomb monolith (470 m$^2$/g and 0.32 cm$^3$/g). These differences are attributed to the effect of the polymeric template on the transformations occurring during the carbonization step. The polymeric molds decompose in inert atmosphere during the thermal treatment releasing hydrocarbons that interact with the phenol-formaldehyde resin, which is being converted into carbon at the same time. This interaction affects the final porosity of the material, and differences observed between the honeycomb and the circular-based counterpart porosity can be ascribed to the amount and distribution of the templating polymer embedded into the polymerized matrix, which differs for each design. Namely, there is more polymer density in the non-conventional circular-channeled polymerizing mixture than in the honeycomb design, which explains the porosity outcomes. This effect was also observed in our previous studies [33].
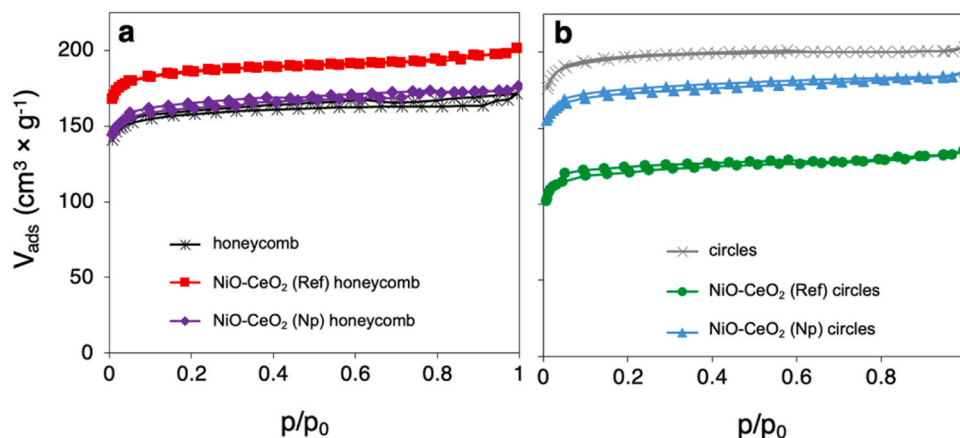
The porosity of the bare carbon monoliths changes upon the loading of the active phases, and differences depend on the monolith design and on the active phase type. These changes can be attributed to the local oxidation of the carbon by ceria oxygen, prone to occur even under inert gas. It is difficult to observe clear trends in these changes of porosity, since they depend on several variables, such us the intrinsic oxidation capacity of the NiO-CeO$_2$ active phase, the local contact between the active phase and carbon and the distribution of the active phase into the carbon network.

Finally, CO$_2$ adsorption at 0 °C was conducted to characterize the narrowest porosity (<0.5 nm) of the bare and active phase-loaded carbon monoliths (Fig. 11). By applying the Dubinin-Radushkevich equation, the micropore volume (V$_{CO2}$) was assessed. In this case, only a small decrease of the ultra-microporosity is observed in the NiO-CeO$_2$ (Ref) circles catalyst with regards to the rest of the materials. This indicates that the effects of the polymer mold decomposition and local oxidation of the carbon by NiO-CeO$_2$ during carbonization did not affect significantly the narrow porosity characterized by CO$_2$ adsorption, but the porosity in a broader range.

The crystallinity of the catalysts was studied by XRD and results are included in Fig. 12.

NiO peaks at 37°, 43° and 63°, respectively [8], are observed in the pure active phases NiO-CeO$_2$ (Np) and NiO-CeO$_2$ (Ref) but not in the supported monoliths due to the diluting effect of carbon. On the contrary, the main peaks of the fluorite structure of CeO$_2$ located at 28.5°, 33.9°, 47.8° and 56.2° [35] are observed in all diffractograms. As expected, peaks corresponding to the NiO-CeO$_2$ (Np) active phase are broader and less intense than those obtained with NiO-CeO$_2$ (Ref), which is in agreement with the smaller particle size of the former. On the other hand, there are no significant differences in the diffractograms obtained before (fresh) and after the catalytic tests (spent), confirming the robustness and stability of the crystallinity of the active phases (Table 3).

**Table 2**

Textural features of the fabricated monoliths with and without NiO-CeO$_2$ loading.

| Sample | S$_{BET}$ (m$^2$/g) | V$_{CO2}$ (cm$^3$/g) | Average pore size (nm) |
|---|---|---|---|
| Honeycomb | 470 | 0.32 | 1.38 |
| Circles | 584 | 0.37 | 1.41 |
| NiO-CeO$_2$ (Ref) honeycomb | 553 | 0.36 | 1.46 |
| NiO-CeO$_2$ (Np) honeycomb | 483 | 0.32 | 1.41 |
| NiO-CeO$_2$ (Ref) circles | 367 | 0.28 | 1.42 |
| NiO-CeO$_2$ (Np) circles | 516 | 0.35 | 1.41 |



**Fig. 10.** N$_2$ adsorption-desorption isotherms of (a) honeycomb monoliths; and (b) circles monoliths.
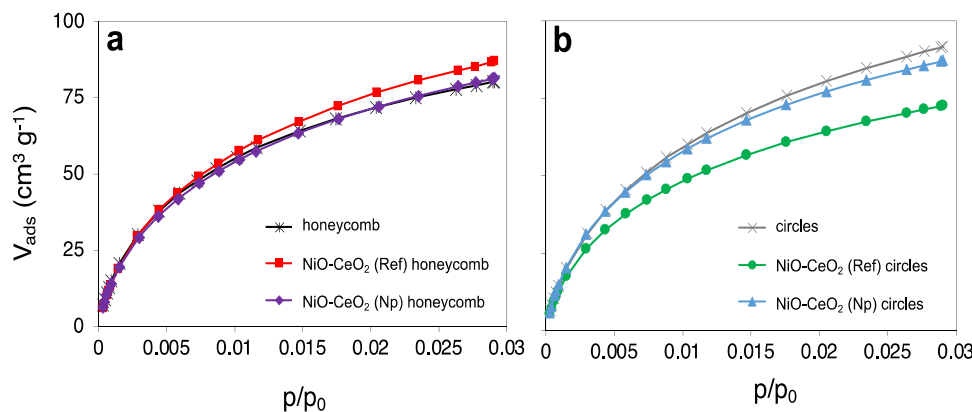
**Fig. 11.** $CO_2$ adsorption isotherms of (a) honeycomb; (b) circular monoliths.
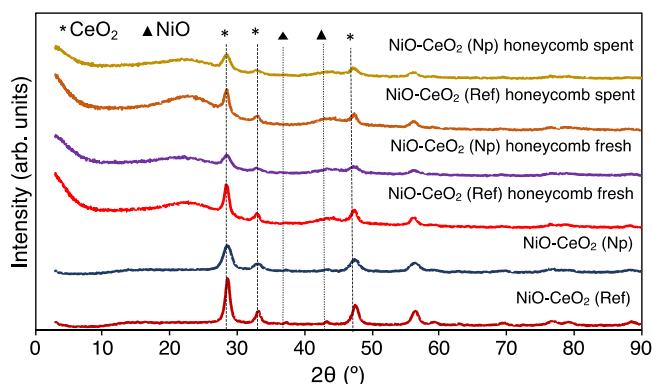


**Fig. 12.** X-ray diffractograms of the powder active phases and the monolithic catalysts before and after reaction.

**Table 3**

Crystalline features of $CeO_2$ phase (Scherrer) calculated using peak centered at ca. $2\theta= 28.5°$ from the X-ray diffractograms.

| Sample | Crystallite size (nm) | Lattice parameter (nm) |
|---|---|---|
| NiO-CeO$_2$ (Ref) | 11 | 0.5404 |
| NiO-CeO$_2$ (Np) | 6 | 0.5412 |
| NiO-CeO$_2$ (Ref) honeycomb fresh | 11 | 0.5425 |
| NiO-CeO$_2$ (Np) honeycomb fresh | 7 | 0.5420 |
| NiO-CeO$_2$ (Ref) honeycomb spent | 11 | 0.5425 |
| NiO-CeO$_2$ (Np) honeycomb spent | 7 | 0.5458 |

As a summary of this characterization section, XRD confirms the expected differences between nanoparticles and reference active phases. It can be concluded that the distribution of the active phases into the carbon monoliths depends on the particle size of the active phase. Nanoparticles are more dispersed into the carbon network than the larger particles of the active phase prepared without size control, which preferentially remain on the monoliths channels surface. This different distribution of the active phases into the carbon supports affects the carbon macroporosity determined by Hg intrusion. The microporosity determined by $N_2$ adsorption is also affected, but in this case changes cannot be attributed to introduction of the active phases into microporosity because the primary particles of the active phases are larger than those micropores.

## 4. Conclusions

The $CO_2$ methanation performance of carbon supported-NiO-CeO$_2$ catalysts has been studied with different monolith design and particle size distribution. The carbon monoliths with different designs have been manufactured using 3D printed polymer templates where NiO-CeO$_2$ nanoparticles and particles with uncontrolled particle size have been loaded to.

Two monolith designs were fabricated, a conventional parallel-channeled structure (honeycomb) and a complex 3D network of non-linear channels built upon interconnected circular sections (circles). It is confirmed that the circles design improves gas diffusion, which is attributed to turbulences spurred along the reactant gas path.

Regardless of the carbon monolith design, the activity of nano-particles ($\sim$ 7 nm) activity is higher at low temperatures (T $<$ 300 ºC), when reaction rate is controlled by intrinsic kinetics, than that of the counterpart catalysts prepared with the uncontrolled-size active phase.

On the contrary, once the $CO_2$ methanation rate increases and gas diffusion (external and/or internal) significantly affects reaction rate (T $>$ 300 ºC), the catalysts prepared with the uncontrolled size active phase achieve higher $CH_4$ production.

SEM and Hg intrusion characterization evidence that nanoparticles are more dispersed into the carbon matrix of the monolithic supports than larger particles of the uncontrolled size active phase, which tend to accumulate on the channels surface being more easily accessible by reactant molecules under mass transfer control.

## Author contributions

The manuscript was written through contributions of all authors. All authors have given approval to the final version of the manuscript. All authors contributed equally.

## CRediT authorship contribution statement

**I. Martínez-López:** Writing - Original Draft, Investigation, Formal analysis, Data Curation; **J.C. Martínez-Fuentes:** Investigation; **J. Bueno-Ferrer:** Investigation, Validation; **A. Davó-Quiñonero:** Data Curation, Writing - Review & Editing, Supervision, Validation; **E. Guillén-Bas:** Supervision, Investigation; **E. Bailón-García:** Conceptualization, Supervision; **D. Lozano-Castelló:** Project administration, Funding acquisition, Resources; **A. Bueno-López:** Writing - Review & Editing, Project administration, Funding acquisition, Resources

## Declaration of Competing Interest

The authors declare the following financial interests/personal relationships which may be considered as potential competing interests:

## Data availability

Data will be made available on request.

## Acknowledgments

## References

[1] A. Malara, P. Frontera, P. Antonucci, A. Macario, Smart recycling of carbon oxides: current status of methanation reaction, Curr. Opin. Green Sustain. Chem. 26 (2020) 100376–100382, https://doi.org/10.1016/j.cogsc.2020.100376.

[2] F. Calise, F.L. Cappiello, L. Cimmino, M. Dentice d'Accadia, M. Vicidomini, Dynamic simulation and thermoeconomic analysis of a power to gas system, Renew. Sustain. Energy Rev. 187 (2023) 113759–113774, https://doi.org/10.1016/j.rser.2023.113759.

[3] M. Thema, F. Bauer, M. Sterner, Power-to-gas: electrolysis and methanation status review, Renew. Sustain. Energy Rev. 112 (2019) 775–787, https://doi.org/10.1016/j.rser.2019.06.030.

[4] J. Ashok, S. Pati, P. Hongmanorom, Z. Tianxi, C. Junmei, S. Kawi, A review of recent catalyst advances in CO$_2$ methanation processes, Catal. Today 356 (2020) 471–489, https://doi.org/10.1016/j.cattod.2020.07.023.

[5] W.J. Lee, C. Li, H. Prajitno, J. Yoo, J. Patel, Y. Yang, S. Lim, Recent trend in thermal catalytic low temperature CO2 methanation: a critical review, Catal. Today 368 (2021) 2–19, https://doi.org/10.1016/j.cattod.2020.02.017.

[6] A. Ricca, L. Truda, V. Palma, Study of the role of chemical support and structured carrier on the CO$_2$ methanation reaction, Chem. Eng. J. 377 (2019) 120461, https://doi.org/10.1016/j.cej.2018.11.159.

[7] N. Engelbrecht, S. Chiuta, R.C. Everson, D.W.J.P. Neomagus, Hein G. Bessarabov, Experimentation and CFD modelling of a microchannel reactor for carbon dioxide methanation, Chem. Eng. J. 313 (2017) 847–857, https://doi.org/10.1016/j.cej.2016.10.131.

[8] S. Fujita, H. Terunuma, M. Nakamura, N. Takezawa, Mechanisms of methanation of carbon monoxide and carbon dioxide over nickel, Ind. Eng. Chem. Res. 30 (1991) 1146–1151, https://doi.org/10.1021/ie00054a012.

[9] A.E. Aksoylu, A.N. Akin, Z.I. Önsan, D.L. Trimm, Structure/activity relationships in coprecipitated nickel-alumina catalysts using CO$_2$ adsorption and methanation, Appl. Catal. A Gen. 145 (1996) 185–193, https://doi.org/10.1016/0926-860X(96)00143-3.

[10] M. Yamasaki, H. Habazaki, T. Yoshida, E. Akiyama, A. Kawashima, K. Asami, K. Hashimoto, M. Komori, K. Shimamura, Compositional dependence of the CO$_2$ methanation activity of Ni/ZrO$_2$ catalysts prepared from amorphous NiZr alloy precursors, Appl. Catal. A Gen. 163 (1997) 187–197, https://doi.org/10.1016/S0926-860X(97)00142-7.

[11] Q. Pan, J. Peng, T. Sun, S. Wang, S. Wang, Insight into the reaction route of CO$_2$ methanation: promotion effect of medium basic sites, Catal. Commun. 45 (2014) 74–78, https://doi.org/10.1016/J.CATCOM.2013.10.034.

[12] Á. Szamosvölgyi, T. Rajkumar, A. Sápi, I. Szenti, M. Ábel, J.F. Gómez-Pérez, K. Baán, Z. Fogarassy, E. Dodony, B. Pécz, S. Garg, J. Kiss, Á. Kukovecz, Z. Kónya, Interfacial Ni active sites strike solid solutional counterpart in CO$_2$ hydrogenation, Environ. Technol. Innov. 27 (2022) 102747–102759, https://doi.org/10.1016/j.eti.2022.102747.

[13] Y. Yu, Z. Bian, J. Wang, Z. Wang, W. Tan, Q. Zhong, S. Kawi, CO$_2$ hydrogenation to CH$_4$ over hydrothermal prepared ceria-nickel catalysts: performance and mechanism study, Catal. Today 424 (2023) 113345–113354, https://doi.org/10.1016/j.cattod.2021.04.002.

[14] T. Shohei, S. Teruyuki, K. Hiromichi, H. Takahide, K. Ryuji, Ni/CeO$_2$ catalysts with high CO$_2$ methanation activity and high CH$_4$ selectivity at low temperatures, Int. J. Hydrog. 37 (2012) 5527–5531.

[15] P.A.U. Aldana, F. Ocampo, K. Kobl, B. Louis, F. Thibault-Starzyk, M. Daturi, P. Bazin, S. Thomas, A.C. Roger, Catalytic CO$_2$ valorization into CH$_4$ on Ni-based ceria-zirconia. Reaction mechanism by operando IR spectroscopy, Catal. Today 215 (2013) 201–207, https://doi.org/10.1016/J.CATTOD.2013.02.019.

[16] Y. Du, C. Qin, Y. Xu, D. Xu, J. Bai, G. Ma, D. Mingyue, Ni nanoparticles dispersed on oxygen vacancies-rich CeO$_2$ nanoplates for enhanced low-temperature CO$_2$

[17] A. Cárdenas-Arenas, A. Quindimil, A. Davó-Quiñonero, E. Bailón-García, D. Lozano-Castelló, U. De-La-Torre, B. Pereda-Ayo, J.A. González-Marcos, J. R. González-Velasco, A. Bueno-López, Design of active sites in Ni/CeO$_2$ catalysts for the methanation of CO$_2$: tailoring the Ni-CeO$_2$ contact, Appl. Mater. Today 19 (2020) 100591–100603, https://doi.org/10.1016/J.APMT.2020.100591.

[18] A.T. Bell, The impact of nanoscience on heterogeneous catalysis, Science 299 (2003) 1688–1691, https://doi.org/10.1126/science.1083671.

[19] B. Roldan Cuenya, F. Behafarid, Nanocatalysis: size- and shape-dependent chemisorption and catalytic reactivity, Surf. Sci. Rep. 70 (2015) 135–187, https://doi.org/10.1016/j.surfrep.2015.01.001.

[20] C. Vogt, E. Groeneveld, G. Kamsma, M. Nachtegaal, L. Lu, C.J. Kiely, P.H. Berben, F. Meirer, B.M. Weckhuysen, Unravelling structure sensitivity in CO$_2$ hydrogenation over nickel, Nat. Catal. 1 (2018) 127–134, https://doi.org/10.1038/s41929-017-0016-y.

[21] A. Cárdenas-Arenas, H.S. Cortés, E. Bailón-García, A. Davó-Quiñonero, D. Lozano-Castelló, A. Bueno-López, Active, selective and stable NiO-CeO$_2$ nanoparticles for CO$_2$ methanation, Fuel Process. Technol. 212 (2021) 106637–106645, https://doi.org/10.1016/J.FUPROC.2020.106637.

[22] E. Poggio-Fraccari, A. Abele, N. Zitta, J. Francesconi, F. Mariño, CO removal for hydrogen purification via water gas shift and COPROX reactions with monolithic catalysts, Fuel 310 (2022) 122419–122428, https://doi.org/10.1016/j.fuel.2021.122419.

[23] C.C. Díaz, M.P. Yeste, H. Vidal, J.M. Gatica, L.E. Cadús, M.R. Morales, In situ generation of Mn$_{1-x}$Ce$_x$ system on cordierite monolithic supports for combustion of n-hexane. effects on activity and stability, Fuel 262 (2020) 116564–116576, https://doi.org/10.1016/j.fuel.2019.116564.

[24] S. Zhao, K. Song, R. Jiang, D. Ma, H. Long, J.-W. Shi, Sm-modified Mn-Ce oxides supported on cordierite as monolithic catalyst for the low-temperature reduction of nitrogen oxides, Catal. Today 423 (2023) 113966–113976, https://doi.org/10.1016/j.cattod.2022.11.027.

[25] Z. Chen, Z. Li, J. Li, C. Liu, C. Lao, Y. Fu, C. Liu, Y. Li, P. Wang, Y. He, 3D printing of ceramics: a review, J. Eur. Ceram. Soc. 39 (2019) 661–687, https://doi.org/10.1016/J.JEURCERAMSOC.2018.11.013.

[26] L.R. Radovic, Physicochemical properties of carbon materials: a brief overview, in: P. Serp, J.L. Figueiredo (Eds.), Carbon Materials for Catalysis, John Wiley & Sons, Inc, 2008, pp. 1–44, https://doi.org/10.1002/9780470403709.ch1.

[27] M.M. Titirici, R.J. White, N. Brun, V.L. Budarin, D.S. Su, F. Del Monte, J.H. Clark, M.J. MacLachlan, Sustainable carbon materials, Chem. Soc. Rev. 44 (2015) 250–290, https://doi.org/10.1039/c4cs00232f.

[28] Z. Zhang, Y. Zhang, X. Mu, J. Du, H. Wang, B. Huang, J. Zhou, X. Pan, E. Xie, The carbonization temperature effect on the electrochemical performance of nitrogen-doped carbon monoliths, Electrochim. Acta 242 (2017) 100–106, https://doi.org/10.1016/j.electacta.2017.05.016.

[29] S. Reljic, C. Cuadrado-Collados, J. Farrando-Perez, E.O. Jardim, M. Martinez-Escandell, J. Silvestre-Albero, Carbon-based monoliths with improved thermal and mechanical properties for methane storage, Fuel 324 (2022) 124753–124761, https://doi.org/10.1016/j.fuel.2022.124753.

[30] M. Yates, J. Blanco, P. Avila, M.P. Martin, Honeycomb monoliths of activated carbons for effluent gas purification, Microporous Mesoporous Mater. 37 (2000) 201–208, https://doi.org/10.1016/S1387-1811(99)00266-8.

[31] J.M. Gatica, J.M. Rodríguez-Izquierdo, D. Sánchez, C. Ania, J.B. Parra, H. Vidai, Extension of preparation methods employed with ceramic materials to carbon honeycomb monoliths, Carbon 42 (2004) 3251–3254, https://doi.org/10.1016/J.CARBON.2004.06.040.

[32] K.P. Gadkaree, M. Jaroniec, Pore structure development in activated carbon honeycombs, Carbon 38 (2000) 983–993, https://doi.org/10.1016/S0008-6223(99)00204-3.

[33] A. Davó-Quiñonero, D. Sorolla-Rosario, E. Bailón-García, D. Lozano-Castelló, A. Bueno-López, Improved asymmetrical honeycomb monolith catalyst prepared using a 3D printed template, J. Hazard. Mater. 368 (2019) 638–643, https://doi.org/10.1016/j.jhazmat.2019.01.092.

[34] C.Y. Chaparro-Garnica, A. Davó-Quiñonero, E. Bailón-García, D. Lozano-Castelló, A. Bueno-López, Design of monolithic supports by 3D printing for its application in the preferential oxidation of CO (CO-PrOx), ACS Appl. Mater. Interfaces 11 (2019) 36763–36773, https://doi.org/10.1021/acsami.9b12731.

[35] C.Y. Chaparro-Garnica, E. Bailón-García, A. Davó-Quiñonero, D. Lozano-Castelló, A. Bueno-López, Sponge-like carbon monoliths: porosity control of 3D-printed carbon supports and its influence on the catalytic performance, Chem. Eng. J. 432 (2022) 134218–134227, https://doi.org/10.1016/j.cej.2021.134218.

[36] C.Y. Chaparro-Garnica, E. Bailón-García, A. Davó-Quiñonero, P. Da Costa, D. Lozano-Castelló, A. Bueno-López, High performance tunable catalysts prepared by using 3D printing, Materials 14 (2021) 5017–5029, https://doi.org/10.3390/ma14175017.

[37] C.Y. Chaparro-Garnica, E. Bailón-García, D. Lozano-Castelló, A. Bueno-López, Design and fabrication of integral carbon monoliths combining 3D printing and sol-gel polymerization: effects of the channel morphology on the CO-PROX reaction, Catal. Sci. Technol. 11 (2021) 6490–6497, https://doi.org/10.1039/d1cy01104a.

[38] A. Martínez-Arias, M. Fernández-García, V. Ballesteros, L.N. Salamanca, J. C. Conesa, C. Otero, J. Soria, Characterization of high surface area Zr-Ce (1:1) mixed oxide prepared by a microemulsion method, Langmuir 15 (1999) 4796–4802.

[39] N. Kovacev, S. Li, S. Zeraati-Rezaei, H. Hemida, A. Tsolakis, K. Essa, Effects of the internal structures of monolith ceramic substrates on thermal and hydraulic properties: additive manufacturing, numerical modelling and experimental testing,

Int. J. Adv. Manuf. Technol. 112 (2021) 1115–1132, https://doi.org/10.1007/s00170-020-06493-2.

[40] Y. Li, S. Chen, X. Cai, J. Hong, X. Wu, Y. Xu, J. Zou, B.H. Chen, Rational design and preparation of hierarchical monoliths through 3D printing for syngas methanation, J. Mater. Chem. A 6 (2018) 5695–5702, https://doi.org/10.1039/c8ta01597j.

[41] S. Wild, C. Mahr, A. Rosenauer, T. Risse, S. Vasenkov, M. Bäumer, New perspectives for evaluating the mass transport in porous catalysts and unfolding macro- and microkinetics, Catal. Lett. 153 (2023) 3405–3422, https://doi.org/10.1007/s10562-022-04218-6.

[42] A. Bustinza, M. Frías, Y. Liu, E. García-Bordejé, Mono- and bimetallic metal catalysts based on Ni and Ru supported on alumina-coated monoliths for $CO_2$ methanation, Catal. Sci. Technol. 10 (2020) 4061–4071, https://doi.org/10.1039/D0CY00639D.

[43] J.A. Onrubia-Calvo, A. Quindimil, A. Davó-Quiñonero, A. Bermejo-López, E. Bailón-García, B. Pereda-Ayo, D. Lozano-Castelló, J.A. González-Marcos, A. Bueno-López, J.R. González-Velasco, Kinetics, model discrimination, and parameters estimation of $CO_2$ methanation on highly active Ni/$CeO_2$ catalys, Ind. Eng. Chem. Res. 61 (2022) 10419–10435, https://doi.org/10.1021/acs.iecr.2c00164.

[44] J.M. Thomas, W.J. Thomas, Principles and Practice of Heterogeneous Catalysis, VCH, Weinheim, 1997. ISBN 3-527-29239-X, Preis: 88, – DM.

[45] P. Schneider, P. Mitschka, Intraparticle diffusion and the apparent activation energy, Chem. Eng. Sci. 24 (1969) 1725–1731, https://doi.org/10.1016/0009-2509(69)87037-5.

[46] Z. Bian, Y.M. Chan, Y. Yu, S. Kawi, Morphology dependence of catalytic properties of Ni/$CeO_2$ for $CO_2$ methanation: a kinetic and mechanism study, Catal. Today 347 (2020) 31–38, https://doi.org/10.1016/j.cattod.2018.04.067.

[47] I. Iglesias, A. Quindimil, F. Mariño, U. De-La-Torre, J.R. González-Velasco, Zr promotion effect in $CO_2$ methanation over ceria supported nickel catalysts, Int. J.

Hydrog. Energy 44 (2019) 17101719, https://doi.org/10.1016/j.ijhydene.2018.11.059.

[48] S. Lin, Z. Hao, J. Shen, X. Chang, S. Huang, M. Li, X. Ma, Enhancing the $CO_2$ methanation activity of Ni/$CeO_2$ via activation treatment-determined metal-support interaction, J. Energy Chem. 59 (2021) 334–342, https://doi.org/10.1016/j.jechem.2020.11.011.

[49] Z. Hao, J. Shen, J. Lin, X. Han, X. Chang, J. Liu, M. Li, X. Ma, Decoupling the effect of Ni particle size and surface oxygen deficiencies in $CO_2$ methanation over ceria supported Ni, Appl. Catal. B 286 (2021) 119922–119932, https://doi.org/10.1016/j.apcatb.2021.119922.

[50] M.S. Duyar, A. Ramachandran, C. Wang, R.J. Farrauto, Kinetics of $CO_2$ methanation over Ru/g-$Al_2O_3$ and implications for renewable energy storage applications, J. $CO_2$ Util. 12 (2015) 27–33, https://doi.org/10.1016/j.jcou.2015.10.003.

[51] L. Sun, K. Luo, J. Fan, Numerical investigation on methanation kinetic and flow behavior in full-loop fluidized bed reactor, Fuel 231 (2018) 85–93, https://doi.org/10.1016/j.fuel.2018.05.042.

[52] I. Fuentes, J.P. Mmbaga, R.E. Hayes, F. Gracia, Potential of microreactors for heat transfer efficient $CO_2$ methanation, Chem. Eng. Sci. 280 (2023) 119047–119058, https://doi.org/10.1016/j.ces.2023.119047.

[53] R.P. Chambers, M. Boudart, Lack of dependence of conversion on flow rate in catalytic studies, J. Catal. 6 (1966) 141–145, https://doi.org/10.1016/0021-9517(66)90118-7.

[54] C. Perego, S. Peratello, Experimental methods in catalytic kinetics, Catal. Today 52 (1999) 133–145, https://doi.org/10.1016/s0920-5861(99)00071-1.

[55] C. Ortega, M. Rezaei, V. Hessel, G. Kolb, Methanol to dimethyl ether conversion over a ZSM-5 catalyst: intrinsic kinetic study on an external recycle reactor, Chem. Eng. J. 347 (2018) 741–753, https://doi.org/10.1016/j.cej.2018.04.160.